Title

Material heterogeneity in cancellous bone promotes deformation recovery after mechanical failure

Journal

Proceedings of the National Academy of Sciences of the United States of America, 113(11)

ISSN

0027-8424

Authors

Torres, Ashley M
Matheny, Jonathan B
Keaveny, Tony M
et al.

Publication Date

2016-03-15

DOI

10.1073/pnas.1520539113

Peer reviewed

Material heterogeneity in cancellous bone promotes deformation recovery after mechanical failure

Ashley M. Torres[a,b,1], Jonathan B. Matheny[a,b,1], Tony M. Keaveny[c], David Taylor[d], Clare M. Rimnac[e], and Christopher J. Hernandez[a,b,f,2]

[a]Meinig School of Biomedical Engineering, Cornell University, Ithaca, NY 14853; [b]Sibley School of Mechanical and Aerospace Engineering, Cornell University, Ithaca, NY 14853; [c]Department of Mechanical Engineering, University of California, Berkeley, CA 94720; [d]Department of Mechanical and Manufacturing Engineering, Trinity College Dublin, Dublin 2, Ireland; [e]Department of Mechanical Engineering, Case Western Reserve University, Cleveland, OH 44106; and [f]Hospital for Special Surgery, New York, NY 10021

Edited by David A. Weitz, Harvard University, Cambridge, MA, and approved January 29, 2016 (received for review October 19, 2015)

Many natural structures use a foam core and solid outer shell to achieve high strength and stiffness with relatively small amounts of mass. Biological foams, however, must also resist crack growth. The process of crack propagation within the struts of a foam is not well understood and is complicated by the foam microstructure. We demonstrate that in cancellous bone, the foam-like component of whole bones, damage propagation during cyclic loading is dictated not by local tissue stresses but by heterogeneity of material properties associated with increased ductility of strut surfaces. The increase in surface ductility is unexpected because it is the opposite pattern generated by surface treatments to increase fatigue life in man-made materials, which often result in reduced surface ductility. We show that the more ductile surfaces of cancellous bone are a result of reduced accumulation of advanced glycation end products compared with the strut interior. Damage is therefore likely to accumulate in strut centers making cancellous bone more tolerant of stress concentrations at strut surfaces. Hence, the structure is able to recover more deformation after failure and return to a closer approximation of its original shape. Increased recovery of deformation is a passive mechanism seen in biology for setting a broken bone that allows for a better approximation of initial shape during healing processes and is likely the most important mechanical function. Our findings suggest a previously unidentified biomimetic design strategy in which tissue level material heterogeneity in foams can be used to improve deformation recovery after failure.

biomaterial | bone remodeling | fracture mechanics | advanced glycation end products | cellular solid

Many natural structures achieve a combination of low weight and mechanical properties that surpass what is currently possible with man-made materials (1). A common structural motif in biological materials is a foam-like structure encased within a thin shell, a structure that uses less mass to achieve the same resistance to bending and torsional loads of solid structures (2, 3). Foam core structures are seen in many biological systems including plants, feather stems, and bones (2, 4). In addition to increasing resistance to bending and torsional loads, the foam cores in biological materials must also resist failure from cracks and other damage generated by cyclic loading. However, little is known about the contribution of material toughness to failure in foams and other cellular solids.

Whole bones consist of a dense shell of cortical bone surrounding a foam-like tissue called cancellous bone. Bone tissue itself is a hierarchical composite consisting of a mineral component (primarily impure hydroxyapatite) and an organic polymer component (primarily type I collagen). In bone, tissue level material toughness has been identified as a key mechanism in resisting osteoporosis- and age-related fractures (5). The ability of bone tissue to resist crack growth has been studied predominately in cortical bone and is a result of a combination of intrinsic (ahead of crack tip) and extrinsic (behind crack tip) toughening mechanisms (6–9) resulting in a fracture toughness, K_{IC}, ranging from 2 to 8 MPa·m$^{1/2}$ (6, 10, 11). Advanced glycation end products (AGEs) accumulate in bone tissue over time and have been shown to have a detrimental effect on resistance to crack growth and fracture (12–14). The most influential extrinsic toughening features in cortical bone are associated with a self-healing process called bone remodeling. During bone remodeling, discrete locations of old or damaged tissue are removed and replaced with newly synthesized material (15). Completed remodeling sites have highly mineralized boundaries known as cement lines that contribute to crack deflection, thereby increasing tissue toughness (9, 16).

The great majority of osteoporosis-related fractures occur in regions of the skeleton dominated by cancellous bone, yet little is known about resistance to crack growth in cancellous bone tissue. Cancellous bone has a complex anisotropic microstructure made up of a network of struts called trabeculae (typically 400 μm long and 120 μm thick). Fracture toughness associated with flaws much larger than individual trabeculae (crack length 1 mm or larger) has been shown to be related to overall porosity in cancellous bone (4, 17, 18). Tissue level toughness also influences failure of cancellous bone, but resistance to crack growth within individual trabeculae has not been reported previously, and it is therefore unclear if alterations in tissue level material toughness contribute to osteoporosis- and age-related fractures in regions of cancellous bone.

Here we examine the propagation of tissue damage in cancellous bone during fatigue loading using a 3D imaging approach known as serial milling. We report the propagation of 1,676 locations of tissue damage and the effects of local tissue stresses

Significance

Lightweight structures often use foam cores to achieve high strength and stiffness. Structures that are submitted to cyclic loading with long service lives must also resist crack propagation. We show that the foam-like regions of cancellous bone resist damage propagation by varying material heterogeneity within struts, a strategy that makes the material less susceptible to stress concentrations at the surface and enhances the ability of the structure to recover its initial shape after mechanical failure. The ability to recover deformation after failure improves long-term function of bones after a fracture. Our findings suggest a previously unidentified design strategy of man-made foams in which material heterogeneity can be used to mitigate the effect of local failure to better maintain mechanical function.

Author contributions: A.M.T., J.B.M., C.M.R., and C.J.H. designed research; A.M.T. and J.B.M. performed research; A.M.T. and J.B.M. analyzed data; and A.M.T., J.B.M., T.M.K., D.T., C.M.R., and C.J.H. wrote the paper.

The authors declare no conflict of interest.

This article is a PNAS Direct Submission.

[1]A.M.T. and J.B.M. contributed equally to this work.

[2]To whom correspondence should be addressed. Email: cjh275@cornell.edu.

This article contains supporting information online at www.pnas.org/lookup/suppl/doi:10.1073/pnas.1520539113/-/DCSupplemental.

and stress concentrations on the surface of trabeculae. We find the propagation of tissue damage to be insensitive to local stresses and instead appears to be dominated by heterogeneities in tissue material properties related to accumulation of AGEs. We conclude that tissue level material heterogeneity in cancellous bone enhances deformation recovery of the structure, which promotes recovery of function after injury.

Results

Fatigue Crack Growth Within Trabeculae Is Primarily Driven by Damage Size and Not Local Tissue Stress. We examined the propagation of tissue damage within cancellous bone (Fig. 1*A*) from the fourth lumbar vertebral bodies of 11 human donors (4 male and 7 female; aged 62–88 y). Cylindrical specimens of cancellous bone were submitted to cyclic compression in two bouts of loading. After each bout of loading, specimens were stained for tissue damage (first with xylenol orange and then with calcein; Fig. 1*B*). The applied loading brings the cancellous bone specimen into the tertiary phase of the creep-fatigue curve but does not cause overt failure (specimens remain intact). Three-dimensional fluorescent images of the entire cancellous bone microstructure (8 mm diameter, 4 mm in height) were collected using epifluorescence-based serial milling at a voxel size sufficient to observe tissue damage (0.7 × 0.7 × 5.0 μm voxels; *Materials and Methods* and Fig. S1). The tissue damage examined consisted of microscopic cracks and regions of submicroscopic cracking, which together we refer to as "damage zones." The use of sequential staining made it possible to observe the propagation of damage zones in cancellous bone in situ. We found that 87% of the tissue damage generated during the second bout of loading was due to expansion of an already existing damage zone (i.e., propagation; Fig. 1*C* and Table S1) rather than the initiation of a new damage zone.

Damage growth rates (dc/dN, m/cycle) and local stress intensity factor range (ΔK, MPa$\sqrt{m}$) were determined using the characteristic size of each damage zone (c = the cubed root of damage zone volume) after each bout of loading, the number of cycles between the two bouts of loading, and the local stress range (von Mises) determined from high-resolution finite element models (10-μm elements, 31–98 million elements per model; *Materials and Methods* and Fig. 2*A*). Damage growth rate was assessed once at each of the 49–287 damage zones in each specimen (1,676 damage zones in 11 specimens). This approach differs from traditional fatigue crack growth, which performs multiple measures of crack growth rate during advance of a single crack, an analysis that, to our knowledge, has been performed on only a few dozen cracks in cortical bone (19–21). The observed damage zone propagation was consistent with the stable crack growth rates of small cracks in cortical bone (Fig. 2*D* and Fig. S2). Damage zone growth rate, however, was positively correlated with local stress intensity factor range within each donor (R^2 = 0.51, P < 0.001), although large interindividual variations were observed (color labels on Fig. 2*D*). Damage zone growth rate was closely related to initial damage zone size (Fig. 2*C*) and, interestingly, showed little relationship to local cyclic stress range (Fig. S3). Larger damage zones were more likely to propagate during the second bout of loading; on average, 72% of damage zones created during the first bout of loading went on to propagate during the second bout of loading (Fig. S4).

To further understand the limited association between local tissue stress and damage propagation, we determined the local tissue stresses at damage zones (Fig. S5*A*). The struts within cancellous bone commonly experience bending and torsional loads, leading to the greatest tissue stresses at strut surfaces (22). Tissue stresses at strut surfaces were greatest on the surfaces of trabeculae (Fig. 2*B* and Fig. S5*B*). However, the majority of tissue damage (68%) occurred in the central regions of trabeculae. Damage zone propagation also occurred predominately in the interior of the trabeculae (Fig. 3*C*). Rupture of individual trabeculae, also known as trabecular microfracture, was rarely observed. The percent of trabeculae in a specimen that ruptured ranged from 0.06% to 1.32% (0.47 ± 0.36%, mean ± SD), demonstrating that failure of individual struts was not a common occurrence. In summary, these results demonstrate that damage formed and propagated in the interior of struts despite the fact that the tissue level stresses were greater at surfaces than the interior.

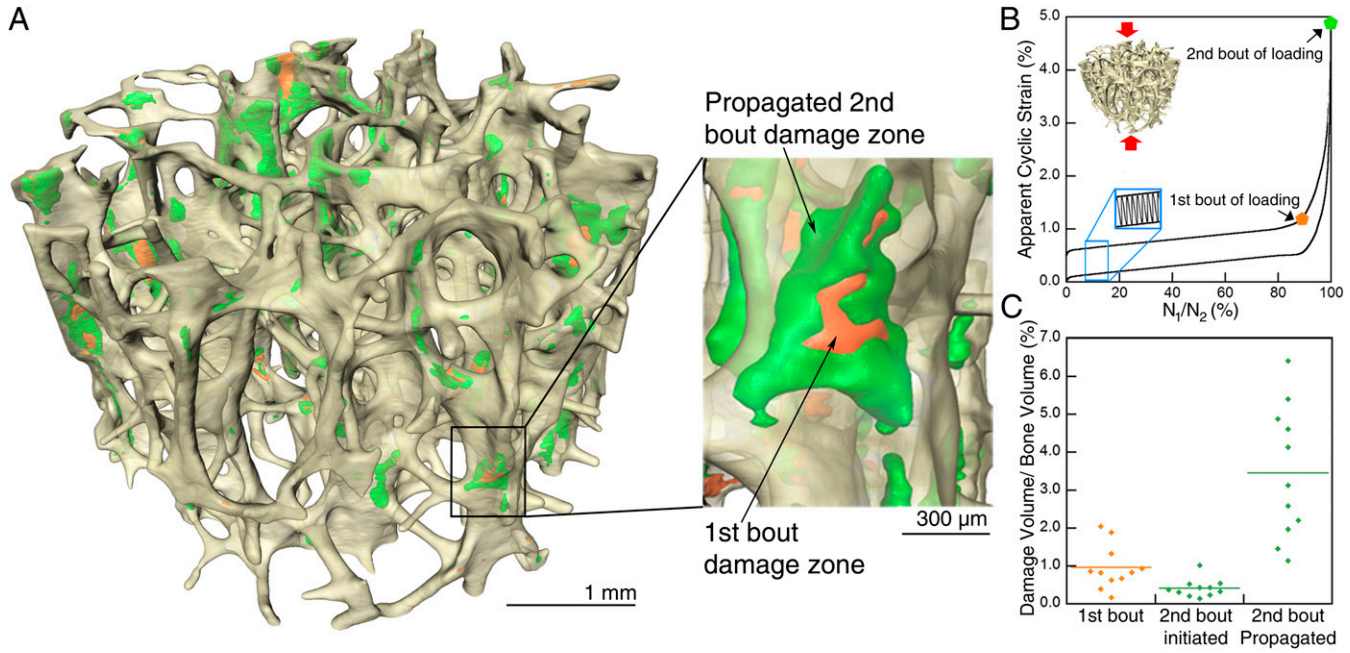

Fig. 1. (*A*) A 3D image of cancellous bone with tissue damage stained is shown. Propagating damage zones display green stain extending from orange stain. (*B*) The minimum and maximum strain per cycle are shown. Cyclic compressive loading was applied to cancellous bone specimens until the start of the tertiary phase of fatigue and a fluorescent stain (orange) was applied to mark damage zones. Cyclic loading was reinstated until 5% applied strain, and a second fluorescent stain (green) was applied. (*C*) 87% percent of the damage volume in the second bout of loading had propagated from preexisting damage.

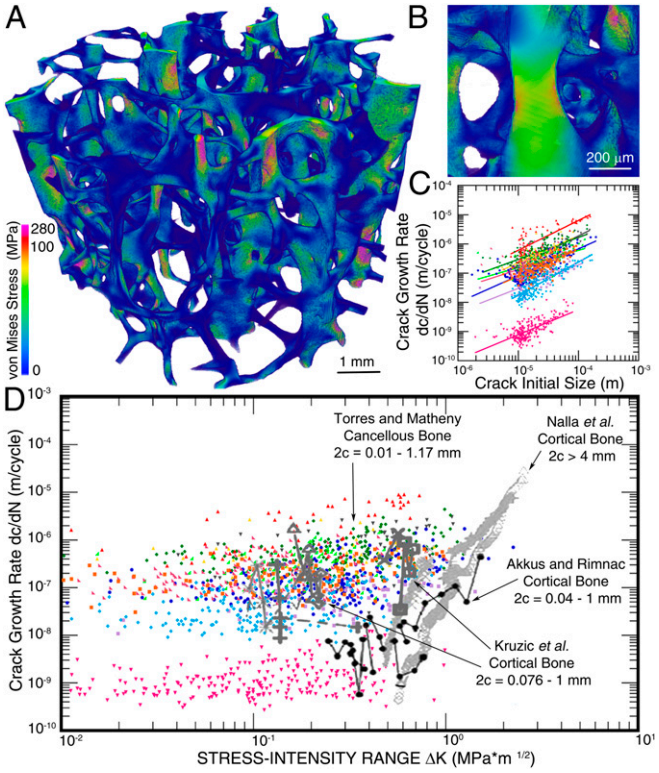

Fig. 2. Fatigue crack growth within cancellous bone. (*A*) The distribution of von Mises stress within trabecular bone is shown. (*B*) Regions of greatest tissue stress were located at surfaces of trabeculae, suggesting that trabeculae experience bending and torsional loading. (*C*) Damage zone growth rate is expressed as the rate of change in damage zone size, *c*, divided by the applied number of cycles, *N*. Damage zone growth was strongly correlated with the size of the damage zone present before the second bout of loading ($P < 0.001$), but showed no correlation to local cyclic stress ($R^2 = 0.006$; Fig. S3). (*D*) Data from the current study (colored points) are shown overlaid with fatigue crack growth measured in cortical bone (a summary of the literature from ref. 19). Positive relationships between crack growth rate (experimental data) and stress intensity range (finite element model data and experimental data) were observed within each specimen ($P < 0.001$). Data points with the same colors are from the same specimen.

Stress Concentrations on Trabecular Surfaces. To confirm our finding that local tissue stress was poorly correlated with damage propagation, we tested the idea that stress concentrations on the trabecular surfaces caused by bone remodeling were preferential locations of damage initiation and propagation. When old or damaged bone tissue is removed during bone remodeling, a cavity is generated on the trabecular surface that can increase local stresses by more than an order of magnitude (23), an increase expected to promote damage initiation and propagation (24). However, we found remodeling cavities (54–111 per specimen; Fig. 3*A*) were preferentially distant from damage zones (Fig. 3*B*). One possible explanation is that trabeculae with cavities experience less stress because load is distributed preferentially to more robust trabeculae that do not have cavities. Additionally there is evidence that the generation of remodeling cavities in vivo occurs primarily on trabeculae experiencing less load (25). However, in our analysis, stresses at remodeling cavities were similar to those at other trabecular surfaces (Fig. S6), demonstrating that trabeculae with cavities were not underloaded. Hence, we conclude that geometric discontinuities associated with the cavities did not lead to the creation or propagation of damage zones. To further assess the unexpected negative correlation between cavities and damage zones, we repeated our analysis considering only the cavities with the largest gross stress concentration factor (greatest ratio of cavity depth to strut thickness). The deepest cavities were even less likely to be near damage zones compared with all of the cavities ($P < 0.05$; Fig. S7). The results indicate that geometric discontinuities such as remodeling cavities have little effect on damage zone initiation or propagation.

Patterns of Tissue Damage Reflect Accumulation of AGEs. To determine whether patterns of material heterogeneity were consistent with regions of damage propagation, we determined the distribution of AGEs in cancellous bone from the same donor cohort. AGEs accumulate in bone tissue over time, and are found in higher concentrations in regions of bone tissue that has been present in an individual for a longer period. AGEs have been associated with nonenzymatic collagen cross-linking and increased tissue level brittleness (26, 27). Higher concentrations of fluorescent AGEs were present in the central regions of the trabeculae (Fig. 4 *A* and *B*). In summary, the presence of fluorescent AGEs, a factor associated with reduced ductility, was greater in the same regions where microscopic tissue damage was more likely to occur.

Discussion

This work provides, to our knowledge, the first experimental analysis of damage propagation within the struts of an open cell foam. The findings demonstrate that accumulation of tissue damage in cancellous bone is predominately the result of propagation from previously existing damage and that propagation of tissue damage occurs distant from regions of high stress due to material heterogeneity. As a result, the likelihood that a damage site will propagate is related to damage zone size instead of the magnitude of the local stress. Small damage events are less likely to propagate, whereas all large damage sites propagate. The results are consistent with the concept that failure of cancellous bone under fatigue is a localized process; once damage forms in a location, additional accumulation of tissue damage is a result of propagation rather than the initiation of new damage sites.

Stress concentration features that are physically small can be ineffective at initiating cracks (28), a fact that would suggest that the locations of damage zones might be indifferent to the presence of remodeling cavities. Damage zones were not found near remodeling cavities; instead, we found that damage propagation was preferentially distant from surfaces with remodeling cavities, implying that differences in tissue material properties at surfaces and the interior are dominating damage propagation. The accumulation of tissue damage in the centers of trabeculae is also consistent with variation in material properties between material at the surface and the interstitial material in the interior of trabeculae. The central interstitial regions of trabeculae have been present longer in the body because bone remodeling initiates at trabecular surfaces. Tissue present in the body longer accumulates greater amounts of AGEs and associated increases in collagen cross-links, as well as altered in mineral composition (increased degree of mineralization and crystallinity), traits that have been associated with increased hardness (29, 30), increased brittleness (27), and reduced ductility (9, 14) of bone material. The current study directly demonstrates increased accumulation of AGEs in the centers of trabeculae, suggesting that reductions in ductility and fracture toughness associated with increased nonenzymatic collagen cross-linking are the likely causes of observed damage patterns. Hence, our observations that damage zones initiate and propagate preferentially distant from cavities and strut surfaces are consistent with the idea that material heterogeneity, specifically increased surface ductility compared with the interior of trabeculae, directs damage propagation.

The observation that cancellous bone displays a more ductile surface and less ductile center was surprising in that it contrasts with surface treatment strategies used to increase fatigue life of man-made materials via surface hardening treatments (31). The presence of a more ductile surface provides two key functional advantages to a biological foam. First, the presence of more ductile trabecular surfaces makes the material less sensitive to

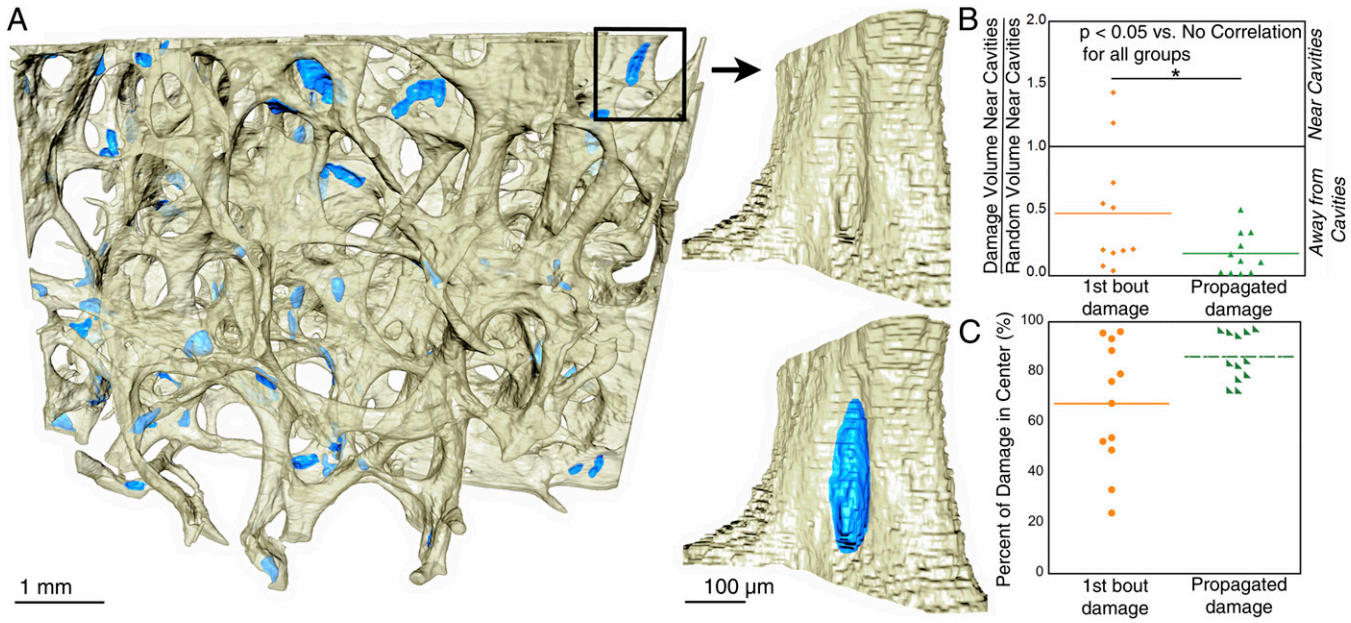

Fig. 3. Tissue damage caused by fatigue loading is distant from stress concentrations generated by bone remodeling. (*A*) Remodeling cavities were traced manually and (*B*) damage zones were less likely to be near cavities than regions selected at random (the ratio is less than 1.0). (*C*) Damage initiated and propagated primarily in the interstitial regions in the center of trabeculae (more than the average depth of remodeling events, 30 μm).

surface flaws and stress concentrations that are unavoidable in biological materials. Without this pattern in tissue heterogeneity, stress concentrations caused by self-healing processes such as bone remodeling could promote failure in cancellous bone. Hence, our findings contradict a long-held assumption that cavities generated by the activity of osteoclasts during the bone remodeling process weaken cancellous bone (24, 32). Second, the presence of a more ductile strut surface forces tissue damage and associated permanent deformations into strut centers. Deformations in struts caused by bending and torsion (the primary loading modes experienced by trabeculae) are small near strut centers (neutral axis/center of twist). As a result, permanent deformations caused by tissue damage in strut centers are much smaller than would be expected if damage were instead present at strut surfaces. On unloading, struts that accumulate tissue damage in the center (where stresses are lower) will recover more deformation from bending and torsion than struts accumulating damage at surfaces. Improved recovery of deformation of individual struts then leads to improved recovery of deformation of the entire foam structure.

Cancellous bone has long been recognized for the ability to recover large amounts of deformation after an overload; specimens compressed well beyond ultimate strain typically recover 61–94% of applied deformation (33–35). The ability to recover deformation in cancellous bone allows for recovery of shape of whole bone after a fracture, and is therefore a passive mechanism of setting or reducing a fracture. By immediately recovering deformation of the whole bone, subsequent self-healing will maintain a structure more similar to the initial bone shape and lead to better function postinjury (33).

The ability of cancellous bone to recover deformation after failure provides a compelling answer to a long-standing question: why do bones have foam-like regions at all? A common explanation for the presence of a foam core in bone is to improve flexural and torsional rigidity and prevent buckling (crimping) (2). However, in long bones the foam-like cancellous bone is present at the

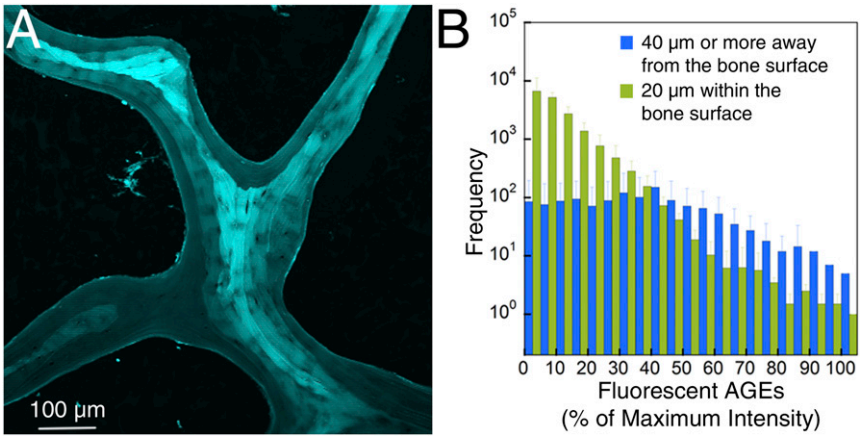

Fig. 4. AGEs in cancellous bone are primarily found distant from the trabecular surface. (*A*) Fluorescence image of decalcified human vertebral cancellous bone. Regions of increased brightness indicate accumulation of AGEs. (*B*) The pixel intensity 40 μm or more away from the surface (blue) and within 20 μm of the bone surface (green) for a donor. The brightest regions were more than 40 μm away from the surface, indicating high AGE content occurs primarily in the center of trabeculae.

ends of the bones near the joints where they would provide relatively little contribution to flexural rigidity and resistance to buckling. The second common explanation for the presence of cancellous bone is improved energy absorption at joints, but energy absorption per unit mass is less in cancellous bone than in solid cortical bone (36). In contrast, recovery of bone shape after fracture, especially at the joints where cancellous bone is most common, is key to enabling effective healing and locomotion after mechanical failure. We suggest that cancellous bone does not so much improve stiffness, strength and energy absorption, but improves performance of the whole bone after failure.

The observed failure mechanisms of cancellous bone provide an attractive strategy for the design of biomimetic materials. Additive manufacturing techniques have achieved materials with designed microstructures that display large amounts of deformation recovery (3). These strategies, however, concentrate on microstructural heterogeneity and mechanical performance before failure but do not necessarily consider material heterogeneity and performance of the component after failure has occurred (1, 2). Lightweight, man-made components using foams treated to increase surface ductility have the potential to continue to provide some mechanical function after overt failure, thereby providing longer service life in cases where replacement and repair are not immediately possible.

Materials and Methods

Specimen Collection. The fourth lumbar vertebral bodies from 11 deceased human donors (4 male and 7 female; aged 62–88 y) were acquired from a nonprofit human tissue bank [National Disease Research Interchange (NDRI)]. Cylindrical cores of cancellous bone aligned in the superior-inferior direction (nominally 8 mm in diameter and 27 mm in length) were dissected from each vertebral body. Specimens were wrapped in saline-soaked gauze and stored in airtight tubes at −20 °C before mechanical testing. Bone marrow was removed with a low-pressure water jet. Each specimen was press fit into cylindrical brass end-caps and secured with cyanoacrylate glue (Loctite 401). Specimens were stored overnight at 4 °C while hydrated with saline-soaked gauze to allow the glue to cure.

Mechanical Testing. Specimens were submitted to cyclic compressive loading in two separate cyclic bouts. Mechanical testing was performed at room temperature (23 °C). To maintain hydration during fatigue testing, specimens were kept hydrated with physiologically buffered saline (pH 7.4). Strain was measured with a 25-mm gauge length extensometer (MTS) attached to the specimen's end-caps. Applied load was measured with a load cell (100-lb capacity, SSM-100; Transducer Techniques). Before each bout of loading, 10 preconditioning cycles between 0% and 0.1% strain at a rate of 0.5%/s were applied. Fatigue loading was applied cyclically between 0 N and a compressive load corresponding to $\sigma = E_0$* 0.0035 mm/mm at a 4-Hz haversine waveform, where σ is stress and E_0 is the initial Young's modulus of the specimen (determined during preconditioning cycles; Fig. S8*A*). The first bout of fatigue loading was stopped before overt failure by detecting rapid changes in the creep-fatigue curve (Fig. 1*B*). Following the first bout of cyclic loading, specimens with end-caps were carefully removed and bulk stained in xylenol orange solution (0.5 mM; Sigma Chemical). Specimens remained fully immersed in xylenol orange for 2 h to label damage zones generated from the first bout of loading (37). The specimens were then rinsed in three 20-min washes of deionized water. The specimens were returned to the testing device, and a second bout of fatigue loading was applied until 5% apparent strain (Fig. 1*B*). A negligible reduction in Young's modulus was caused by interruption of loading (Fig. S8*B*). Following the second bout of loading, specimens were carefully removed from the testing device and bulk stained in calcein solution (0.5 mM; Sigma Chemical) to label damage zones generated during the second bout of loading using the same 2-h incubation period and rinses as the first damage stain (37). Specimens were then removed from the end-caps using a low-speed diamond saw (Isomet; Buehler Ltd) and embedded in methylmethacrylate made opaque with sudan black dye in preparation for image acquisition using serial milling (38).

Microscopic Tissue Damage. Three-dimensional images of bone and fluorescent markers of damage zones were collected using serial milling to achieve a voxel size of 0.7 × 0.7 × 5.0 μm (690 GB per specimen; Fig. S1) (39). Three images of each specimen were collected using different fluorescent filter sets: one channel to visualize bone tissue (350/420 nm, Ex/Em), and one for each of the two fluorescent markers of damage zones (xylenol orange, 545/620 nm; calcein, 470/525 nm). Images collected were segmented by a trained observer and underwent 3D binary morphological operations. Propagating damage zones were identified as regions where the second damage stain was in direct contact with the first damage stain. Remodeling cavities on the bone surfaces were detected by irregular surface texture and traced manually in three dimensions (40). Spatial correlations between damage zones and remodeling cavities were determined as the ratio of damage volume near remodeling cavities (within 8 μm) to that of bone volume selected at random that was found to be near remodeling cavities (41). The characteristic size of each damage zone (c = cubed root of damage zone volume) was determined at the end of the first bout of loading ($c_{initial}$) and at the end of the second bout of loading (c_{final}), and the growth rate was determined as follows:

$$\frac{dc}{dN} = \frac{c_{final} - c_{initial}}{N_{secondbout}},$$

where $N_{secondbout}$ is the number of cycles applied between the first and second bouts of loading.

Finite Element Modeling and Damage Propagation. Three-dimensional images of each specimen, collected before loading using microcomputed tomography (10-μm voxels), were used to generate linear elastic finite element models. Each finite element model consisted of 31–98 million elements and was implemented on the Stampede Supercomputer Cluster (Texas Advanced Computing Center) (42). The tissue Young's modulus for each model was selected so that the stiffness of the finite element model matched that of the apparent Young's modulus determined experimentally (tissue Young's modulus, 13.74 ± 3.25 GPa, mean ± SD). Compression applied at the apparent scale (millimeters) resulted in local regions of compression (Fig. S9*A*) and tension (Fig. S9*B*). The average von Mises stress within each damage zone, along with damage zone length, c, was used to calculate ΔK. Similar results were achieved with other scalar assays of tissue stress/strain.

AGEs. Five cylindrical cores of cancellous bone from the same donor pool (2 male and 3 female; aged 67–88 y) were analyzed for fluorescent AGEs. Specimens were decalcified in a sodium citrate-formic acid solution and then dehydrated. Following dehydration, samples were embedded in paraffin, and 6-μm-thick transverse sections were mounted onto slides. AGEs were observed by auto fluorescence in five sections per sample using a confocal microscope (Zeiss 710, 405/488 nm, Ex/Em) with uniform exposure time (150 ms). Bright field images were used to normalize brightness among fields of view. Images were analyzed using Image J (National Institutes of Health).

ACKNOWLEDGMENTS. We thank Christopher Chapa and Floor Lambers for assistance with specimen preparation. We thank Matthew Goff for assistance with finite element models. This work was supported by National Institute of Arthritis and Musculoskeletal and Skin Diseases of the National Institutes of Health Award AR057362 (principal investigator, C.J.H.). We acknowledge use of human vertebral bodies provided by the National Disease Research Interchange, with support from National Institutes of Health (NIH) Grant 8U42OD011158-22, Cornell's National Science Foundation (NSF) Grant DGE-1144153, NSF Graduate Research Fellowship Program (GRFP) (to A.M.T.), NSF GRFP (to J.B.M.), and a Cornell Colman fellowship (to A.M.T.). Imaging data were acquired in the Cornell Biotechnology Resource Center (BRC)-Imaging Facility using the shared, NIH-funded (S10RR025502) Zeiss LSM 710 Confocal.

1. Wegst UG, Bai H, Saiz E, Tomsia AP, Ritchie RO (2015) Bioinspired structural materials. *Nat Mater* 14(1):23–36.
2. Meyers MA, McKittrick J, Chen P-Y (2013) Structural biological materials: Critical mechanics-materials connections. *Science* 339(6121):773–779.
3. Meza LR, et al. (2015) Resilient 3D hierarchical architected metamaterials. *Proc Natl Acad Sci USA* 112(37):11502–11507.
4. Gibson LJ (2005) Biomechanics of cellular solids. *J Biomech* 38(3):377–399.
5. Ritchie RO, Buehler MJ, Hansma P (2009) Plasticity and toughness in bone. *Phys Today* 62(6):41–47.
6. Nalla RK, Kinney JH, Ritchie RO (2003) Mechanistic fracture criteria for the failure of human cortical bone. *Nat Mater* 2(3):164–168.
7. Koester KJ, Ager JW, 3rd, Ritchie RO (2008) The true toughness of human cortical bone measured with realistically short cracks. *Nat Mater* 7(8):672–677.
8. Launey ME, Buehler MJ, Ritchie RO (2010) On the mechanistic origins of toughness in bone. *Annu Rev Mater Res* 40(1):25–53.
9. Zimmermann EA, et al. (2011) Age-related changes in the plasticity and toughness of human cortical bone at multiple length scales. *Proc Natl Acad Sci USA* 108(35):14416–14421.

10. Zioupos P, Currey JD (1998) Changes in the stiffness, strength, and toughness of human cortical bone with age. *Bone* 22(1):57–66.
11. Akkus O, Jepsen KJ, Rimnac CM (2000) (Microstructural aspects of the fracture process in human cortical bone. *J Mater Sci* 35(24):6065–6074.
12. Ager JW, Balooch G, Ritchie RO (2006) Fracture, aging, and disease in bone. *J Mater Res* 21(08):1878–1892.
13. Wang X, Shen X, Li X, Agrawal CM (2002) Age-related changes in the collagen network and toughness of bone. *Bone* 31(1):1–7.
14. Vashishth D, et al. (2001) Influence of nonenzymatic glycation on biomechanical properties of cortical bone. *Bone* 28(2):195–201.
15. Taylor D, Hazenberg JG, Lee TC (2007) Living with cracks: Damage and repair in human bone. *Nat Mater* 6(4):263–268.
16. Busse B, et al. (2013) Vitamin D deficiency induces early signs of aging in human bone, increasing the risk of fracture. *Sci Transl Med* 5(193):193ra88.
17. Griffith JF, Genant HK (2012) New advances in imaging osteoporosis and its complications. *Endocrine* 42(1):39–51.
18. Cook RB, Zioupos P (2009) The fracture toughness of cancellous bone. *J Biomech* 42(13):2054–2060.
19. Kruzic JJ, Scott JA, Nalla RK, Ritchie RO (2006) Propagation of surface fatigue cracks in human cortical bone. *J Biomech* 39(5):968–972.
20. Nalla RK, Stölken JS, Kinney JH, Ritchie RO (2005) Fracture in human cortical bone: Local fracture criteria and toughening mechanisms. *J Biomech* 38(7):1517–1525.
21. Akkus O, Rimnac CM (2001) Fracture resistance of gamma radiation sterilized cortical bone allografts. *J Orthop Res* 19(5):927–934.
22. Renders GA, Mulder L, van Ruijven LJ, Langenbach GE, van Eijden TM (2011) Mineral heterogeneity affects predictions of intratrabecular stress and strain. *J Biomech* 44(3): 402–407.
23. McNamara LM, Van der Linden JC, Weinans H, Prendergast PJ (2006) Stress-concentrating effect of resorption lacunae in trabecular bone. *J Biomech* 39(4):734–741.
24. Hernandez CJ (2008) How can bone turnover modify bone strength independent of bone mass? *Bone* 42(6):1014–1020.
25. Huiskes R, Ruimerman R, van Lenthe GH, Janssen JD (2000) Effects of mechanical forces on maintenance and adaptation of form in trabecular bone. *Nature* 405(6787): 704–706.
26. Tang SY, Vashishth D (2010) Non-enzymatic glycation alters microdamage formation in human cancellous bone. *Bone* 46(1):148–154.
27. Willett TL, Sutty S, Gaspar A, Avery N, Grynpas M (2013) In vitro non-enzymatic ribation reduces post-yield strain accommodation in cortical bone. *Bone* 52(2):611–622.
28. Taylor D (2007) *The Theory of Critical Distances* (Elsevier, London).
29. Brennan O, Kennedy OD, Lee TC, Rackard SM, O'Brien FJ (2009) Biomechanical properties across trabeculae from the proximal femur of normal and ovariectomised sheep. *J Biomech* 42(4):498–503.
30. Burket JC, et al. (2013) Variations in nanomechanical properties and tissue composition within trabeculae from an ovine model of osteoporosis and treatment. *Bone* 52(1):326–336.
31. Dowling NE (2007) *Mechanical Behaviour of Materials* (Pearson Prentice Hall, Upper Saddle River, NJ), 3rd Ed.
32. Dempster DW (2000) The contribution of trabecular architecture to cancellous bone quality. *J Bone Miner Res* 15(1):20–23.
33. Fyhrie DP, Schaffler MB (1994) Failure mechanisms in human vertebral cancellous bone. *Bone* 15(1):105–109.
34. Keaveny TM, Wachtel EF, Kopperdahl DL (1999) Mechanical behavior of human trabecular bone after overloading. *J Orthop Res* 17(3):346–353.
35. Hernandez CJ, Lambers FM, Widjaja J, Chapa C, Rimnac CM (2014) Quantitative relationships between microdamage and cancellous bone strength and stiffness. *Bone* 66:205–213.
36. Currey JD (2002) *Bones: Structure and Mechanics* (Princeton Univ Press, Princeton).
37. O'Brien FJ, Taylor D, Lee TC (2002) An improved labelling technique for monitoring microcrack growth in compact bone. *J Biomech* 35(4):523–526.
38. Bigley RF, et al. (2008) Validity of serial milling-based imaging system for microdamage quantification. *Bone* 42(1):212–215.
39. Slyfield CR, Jr, et al. (2009) Three-dimensional surface texture visualization of bone tissue through epifluorescence-based serial block face imaging. *J Microsc* 236(1): 52–59.
40. Dempster DW, et al. (2013) Standardized nomenclature, symbols, and units for bone histomorphometry: A 2012 update of the report of the ASBMR Histomorphometry Nomenclature Committee. *J Bone Miner Res* 28(1):2–17.
41. Goff MG, Chang KL, Litts EN, Hernandez CJ (2014) The effects of misalignment during in vivo loading of bone: Techniques to detect the proximity of objects in three-dimensional models. *J Biomech* 47(12):3156–3161.
42. Eswaran SK, Gupta A, Adams MF, Keaveny TM (2006) Cortical and trabecular load sharing in the human vertebral body. *J Bone Miner Res* 21(2):307–314.